



Dual-mode colorimetric/fluorescent chemosensor for $\text{Cu}^{2+}/\text{Zn}^{2+}$ and fingerprint imaging based on rhodamine ethylenediamine bis(triazolyl silsesquioxane)

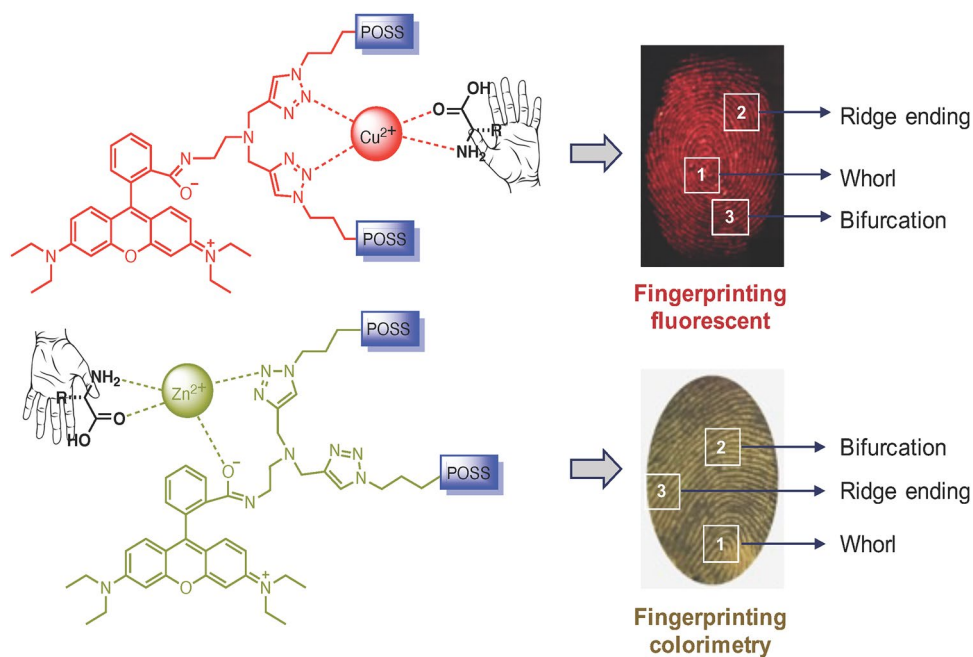
Enock O. Dare^{1,2} · Temilade F. Akinhanmi¹ · J. A. Aremu¹ · Olayide R. Adetunji^{1,6} · Janet T. Bamgbose¹ · Victoria Vendrell-Criado³ · M. Consuelo Jiménez³ · Raúl Pérez-Ruiz³ · Sebastian Bonardd^{4,5} · David Díaz Díaz^{2,4,5}

Received: 25 November 2022 / Accepted: 7 February 2023 / Published online: 16 March 2023
© The Author(s) 2023

Abstract

A novel dual functional and visual rhodamine ethylenediamine bis(triazolyl silsesquioxane) (**RBS**) chemosensor was successfully synthesized using “click” chemistry. The results have unambiguously demonstrated that **RBS** can act in fluorescent and colorimetric sensing of Cu^{2+} and Zn^{2+} by their respective coordination with triazole structures and, more importantly, it has also been found that triazole-amide of **RBS** could turn on chelation-enhanced fluorescence (**CHEF**) of Cu^{2+} . Remarkably, the addition of Cu^{2+} triggered an enhanced fluorescent emission by 63.3-fold ($\phi_F=0.41$), while Zn^{2+} enhanced it 48.3-fold ($\phi_F=0.29$) relative to the original **RBS** ($\phi_F=0.006$) in acetonitrile (MeCN) solvent. The fluorescent limit of detection for Cu^{2+} and Zn^{2+} is similar and fall within 3.0 nM, while under colorimetric sensing the responses were 2.14×10^{-8} and $4.0 \times 10^{-8} \text{ mol L}^{-1}$, respectively. Moreover, the effective sensing profile of **RBS** and extended applications of **RBS**– Cu^{2+} and **RBS**– Zn^{2+} for fingerprinting detection and imaging were observed with adequate sensitivity, stability and legibility under the dual visual responses.

Graphical abstract



Keywords Rhodamine · Silsesquioxane · Chemosensor · Fingerprint imaging

1 Introduction

The design and synthesis of novel nanoscopic molecules that can recognize and detect cations and show specificity for biologically relevant metal ions have gained attention during the last decade [1]. Particularly, Cu^{2+} , Zn^{2+} and Fe^{3+} play vital roles in several biological, environmental and chemical systems. These metal ions are essential trace elements for both plants and animals, including humans. Literature medical data reiterates that excess accumulation of Zn^{2+} has the propensity to alter Cu^{2+} and $\text{Fe}^{2+}/\text{Fe}^{3+}$ absorption in humans and eventually lead to a series of health problems [2]. While several expensive and time-consuming spectroscopic analytical techniques could detect and discriminate Zn^{2+} , Cu^{2+} and $\text{Fe}^{2+}/\text{Fe}^{3+}$ among many other metals [3, 4], a more accurate and sensitive probe would be beneficial for detecting these biologically relevant cations.

Within this context, fluorescent and colorimetric sensors are appropriate alternative probes for Cu^{2+} and Zn^{2+} sensing [5–10]. Among common fluorophores, rhodamine derivatives are widely employed for detection of metal ions due to their variably distinguished properties such as (i) the ability to generate cell- and tissue-permeant labels for biological imaging and sensing, despite the photophysical equilibrium between the non-fluorescent lipophilic closed form and the open form of strongly fluorescent rhodamine derivatives [11–14] and (ii) the ability to re-design a red-shifted longer wavelength absorbance/emission spectrum from a green to pinkish red colour for a fluorogenic and/or chromogenic response [13].

To turn on the fluorescence emission of rhodamine probes, a spirolactam ring must be opened [14]. One of the methods to achieve this consists in introducing a strongly chelating metal ion [15]. Several photoactive moieties, including rhodamine, have been effectively conjugated with appropriate binding units using “click”-generated 1,2,3-triazole-based chemosensors for Zn^{2+} , Cu^{2+} and Fe^{3+} [16–20]. For effective and efficient practical application of rhodamine triazolyl-based fluorogenic probes, photostability is a highly required feature that, unfortunately, remains unresolved. Indeed, we recently pioneered the synthesis of fluorescent-labeled triazolyl polyhedral oligomeric silsesquioxanes (POSS) for applications in forensic science [21, 22]. Taking advantage of the great versatility of the Cu(I)-catalyzed 1,3-dipolar cycloaddition of azides and alkynes (CuAAC), the obtained POSS nanohybrids showed excellent photostability and thermal properties, and were able to image fingerprints with good selectivity, sensitivity and

legibility. Several factors that underpin the candidature of POSS include the photostability showed by its triazolyl hybrids, together with their biocompatibility, facile functionalization and nano-dimensionality (0.5–0.7 nm) [23–27]. As we engaged in unprecedented advances vis-à-vis proof of concept of our ongoing work, we present herein the strategic design and synthesis of novel rhodamine-labeled bis(triazolyl)-POSS (**RBS**) using the popular CuAAC for selective sensing of Cu^{2+} and Zn^{2+} and extended the application for fingerprint imaging via (**RBS-M²⁺**)-amino acid interaction. As far as we are aware, this is also the first example utilizing two binding profiles of bis-triazolyl-POSS rhodamine for dual functionality and visuality.

2 Experimental

2.1 Materials

All chemicals (i.e., rhodamine B, propargyl bromide, sodium azide, ethylenediamine, CuBr, *N,N,N',N'',N'''*-pentamethyldiethylenetriamine (PMDETA) and 3-chloropropyl)hepta(*i*-butyl)octasilsesquioxane) were purchased from Sigma-Aldrich. Stock solutions of various metal ions (20 μM) were prepared from $\text{Zn}(\text{NO}_3)_2$, $\text{Ca}(\text{NO}_3)_2$, $\text{Cd}(\text{OAc})_2 \cdot \text{H}_2\text{O}$, $\text{Cu}(\text{NO}_3)_2$, $\text{Co}(\text{NO}_3)_2$, $\text{Ni}(\text{OAc})_2$, $\text{Pb}(\text{NO}_3)_2$ and $\text{Fe}(\text{NO}_3)_3$. ^1H NMR spectra were recorded on a Bruker Avance 300, 400, 500 MHz spectrometer in CDCl_3 . For the optical responses of RBS to metal ions, phosphate-buffered saline of pH 7.4 was used. ^{13}C NMR was recorded on a Bruker Avance 300 or 400 MHz (resonance frequency: 75 and 101 MHz, respectively) under broadband ^1H decoupling in CDCl_3 . ^{29}Si NMR was recorded in the same manner. Chemical shifts are reported in ppm relative to either tetramethylsilane (TMS) (1H) ($\delta=0$ ppm) as an internal standard or the residual solvent peak of CDCl_3 (^1H NMR: $\delta=7.26$ ppm; ^{13}C NMR: $\delta=77.16$ ppm). FT-IR spectra were obtained with an Agilent Technologies Cary 630 FT-IR spectrometer equipped with Golden Gate Diamond attenuated total reflection (ATR) accessory. Mass data for **RBS** were obtained at Würzburg University with an Exactive Plus Orbitrap Mass Spectrometer from Thermo Scientific. All reactions were monitored by TLC using Merck silica gel plates 60 F254, and visualization was accomplished with short-wavelength UV light (254 nm) and/or upon staining with appropriate stains (anisaldehyde, orthophosphomolybdic acid).

2.2 Synthesis and characterization of compounds

2.2.1 Synthesis of 3-azidopropyl hepta(*i*-butyl)POSS (POSS-azide, **PA**)

POSS-azide (**PA**) was synthesized following a previously described methodology [22]. Briefly, sodium azide (0.436 g, 6.71 mmol, 3 equiv) was added to 3-chloropropyl hepta(*i*-butyl)POSS (2.0 g, 2.24 mmol) in a mixture of dry DMF (70 mL) and dry THF (20 mL) under a dry nitrogen atmosphere. The mixture was stirred at 70 °C for 24 h and the reaction was cooled down at room temperature (RT). The reaction was quenched by adding triturated ice (80 g) to induce precipitation. The obtained product was filtered, dried under vacuum, and recrystallized from a mixture of THF:methanol (1:3, v/v) affording the desired compound as a colorless solid (1.43 g, 2.09 mmol, 81% yield). ¹H NMR (300 MHz, CDCl₃): δ (ppm) = 3.28 (t, 2H), 1.90 (m, 7H), 1.75 (quin, 2H), 0.97 (d, 42H), 0.70 (overlapped, 2H), 0.63 (m, 14H). ¹³C NMR (125 MHz, CDCl₃): δ (ppm) = 52.88, 25.66, 25.69, 23.89, 23.84, 22.46, 22.41, 9.31. ²⁹Si NMR (99 MHz, CDCl₃): δ (ppm) = −67.55, −68.17.

2.2.2 Synthesis of rhodamine–ethylenediamine conjugate (**RED**)

A solution of rhodamine B (500 mg, 1.05 mmol) in dry EtOH (20 μM) was added dropwise to a solution of ethylenediamine (528 μL, 7.88 mmol, 7.5 equiv) in EtOH (1 mL) under vigorous stirring at RT, and the mixture was refluxed for 16 h. Then, it was cooled to RT and the solvent was removed under reduced pressure. The obtained residue was dissolved in CH₂Cl₂ (20 mL) and extracted with water (3 × 15 mL). The combined organic layers were dried over anhydrous Na₂SO₄ and the solvent removed under reduced pressure to afford the desired product as an orange solid (409.5 mg, 0.87 mmol, 81.9% yield). ¹H NMR (300 MHz, CDCl₃): δ (ppm) = 7.92 (m, 1H), 7.46 (m, 2H), 7.11 (m, 1H), 6.46 (s, 1H), 6.44 (s, 1H), 6.38 (d, 2H), 6.28 (dd, 2H), 3.34 (q, 8H), 3.20 (t, 2H), 2.40 (t, 2H), 1.18 (t, 12H); ¹³C NMR (75 MHz, CDCl₃): δ (ppm) = 168.58, 153.42, 153.23, 148.77, 132.35, 131.19, 128.63, 127.99, 123.78, 122.70, 108.10, 105.62, 97.67, 64.88, 44.29, 43.81, 40.74, 12.53.

2.2.3 Synthesis of rhodamine dipropargyl-ethylenediamine conjugate (**REDD**)

REDD was obtained according to the reported procedure [20]. Briefly, rhodamine B-ethylenediamine conjugate (193.4 mg, 0.40 mmol) was dissolved in 30 mL of MeCN. Then, anhydrous K₂CO₃ (110.6 mg, 0.80 mmol, 2 equiv) and KI (6.6 mg, 0.04 mmol, 10 mol %) were added under vigorous stirring and the mixture refluxed

for 30 min. Then, a solution of propargyl bromide (50 μL, 0.80 mmol, 2 equiv) in MeCN (1 mL) was added to the suspension and the mixture was refluxed for 24 h. Then, it was cooled to RT and the solvent removed under reduced pressure. The obtained residue was dissolved in CH₂Cl₂ (30 mL) and washed with water (3 × 20 mL). The combined organic layers were dried over anhydrous Na₂SO₄, filtered, and the solvent removed under reduced pressure. The obtained material was purified by column chromatography affording the desired product as a brown solid (111.8 mg, 0.24 mmol, 57.8% yield). ¹H NMR (300 MHz, CDCl₃): δ (ppm) = 7.89 (m, 1H), 7.42 (m, 2H), 7.07 (m, 1H), 6.44 (d, 2H), 6.38 (d, 2H), 6.26 (dd, 2H), 3.32 (q, 8H), 3.25 (m, 6H), 2.25 (t, 2H), 2.10 (t, 2H), 1.16 (t, 12H); ¹³C NMR (125 MHz, CDCl₃): δ (ppm) = 167.97, 153.45, 153.22, 148.70, 132.26, 131.23, 129.04, 127.95, 123.70, 122.70, 108.21, 105.61, 97.77, 78.78, 73.37, 72.59, 64.76, 53.36, 50.82, 44.36, 41.70, 37.96, 12.50.

2.2.4 Synthesis of rhodamine ethylenediamine bis(triazolyl POSS) (**RBS**)

A DMF/THF (1:1, v/v) solution (10 mL) of **PA** (0.35 g, 4.0 × 10^{−4} mol, 2.2 equiv) was added to a stirred solution of rhodamine dipropargyl-ethylenediamine conjugate (0.1 g, 1.8 × 10^{−4} mol) in THF (5 mL). Then, a suspension of CuBr and PMDETA (50 mol%) in DMF (5 mL) was added under nitrogen atmosphere. The reaction mixture was left under stirring for 24 h at RT. After the solvent was removed under reduced pressure, the obtained product was re-dissolved in CH₂Cl₂, washed with aqueous EDTA (7.44 mL, 0.02 mol) and dried under Na₂CO₃. The resulting product was further purified by column chromatography affording the desired product as a light brown solid (260 mg, 0.11 mmol, 73% yield). ¹H NMR (300 MHz, CDCl₃): δ (ppm) = 0.62–0.69 (−SiCH₂−, SiCH₂CH(CH₃)₂, 32H, overlapped), 0.72–0.97 [(−CH(CH₃)₂)₂, 84H], 1.1–1.9 (−N[CH₂CH₃]₂ rhodamine, 12H), 1.7–1.8 (SiCH₂CH(CH₃)₂, 14H), 1.9–2.0 SiCH₂CH₂CH₂−N, 4H) 3.2–3.4 (−N[CH₂CH₃]₂ rhodamine 8H, NCH₂CH₂−diethylene, 2H, overlapped), 3.6 (N−[CH₂−triazole]₂, 4H), 4.3 ([triazole−CH₂−]₂, 4H), 6.3 (−CH₂NC=O, 2H, spirolactam ring), 7.6 (−[triazole]₂, 2H), 6.4–8.3 (aromatic protons of rhodamine, 10H). ¹³C NMR (125 MHz, CDCl₃): δ (ppm) = 12.62, 12.60, 40.85, 40.87, 43.89, 43.92, 44.34, 65.92, 97.66, 97.69, 108.13, 108.10, 122.74, 123.23, 123.84, 128.69, 131.25, 132.41, 148.80, 153.49, 168.20, 168.66. ²⁹Si NMR (99 MHz, CDCl₃): δ (ppm) = −67.86, −68.34. FT-IR (cm^{−1}): ν(CH) 2992–2891; δ(CH) 1374–1211; ν(C=C) 1658; ν(Si−O−Si) 1134–1022; MS (API-ESI) *m/z*: 2361.9 [M⁺+H]⁺. Elemental analysis: calculated for C₉₈H₁₈₀N₁₀O₂₆Si₁₆ (MW 2362.92) C 47.79, H 7.68, N 5.93; found C 47.92, H 7.74, N 5.89%.

2.3 Photophysical characterization

2.3.1 Absorption measurements

Steady-state absorption spectra were recorded in a JASCO V-630 spectrophotometer. Quartz cells with 1 cm optical path length and 3 mL capacity were employed. Molar coefficient extinction was determined according to the Lambert–Beer law (Eq. 1):

$$\text{Abs} = C \cdot \varepsilon \cdot L, \quad (1)$$

where Abs is the absorbance of the sample, C the concentration (M), and L the optical path length (cm).

2.3.2 Fluorescence experiments

Emission spectra were recorded at 22 °C on a JASCO FP-8500 spectrofluorometer system, provided with a monochromator in the wavelength range of 200–850 nm. From the intersection between normalized excitation and emission spectra, the singlet energy was determined. Fluorescence quantum yields were determined using 9,10-dimethylanthracene as standard ($\phi_{\text{F(Std)}} = 0.95$, EtOH) (Eq. 2):

$$\phi_{\text{F}} = \frac{A_i}{A_{\text{std}}} \cdot \frac{\text{Abs}_{\text{std}}}{\text{Abs}_i} \cdot \frac{n}{n_{\text{std}}} \phi_{\text{F(Std)}}, \quad (2)$$

where A_i is the fluorescence area of the sample, A_{std} is the fluorescence area of standard, Abs and Abs_{std} correspond to the absorbance intensity at excitation wavelength of the sample and standard, respectively, and n is the refraction index of the solution employed. Fluorescence lifetimes were recorded on a Photon Technology International (PTI) fluorometer which includes a pulsed LED excitation source (310 nm), a sample holder and a lifetime detector. For lifetime analysis, EasyLife X software, was used.

2.3.3 Binding constant

The binding constant was determined from a Job plot using Benesi–Hildebrand (B–H) equation [28] (Eq. 3):

$$1/(F - F_0) = (1/K_a[C]) \{1/(F_{\text{max}} - F_0)\} + 1/(F_{\text{max}} - F_0), \quad (3)$$

where F_0 is the emission intensity of the probe **RBS** at maximum ($\lambda = 580$ nm), F is the observed emission intensity at that particular wavelength in the presence of a certain concentration of the analyte (C), F_{max} is the maximum emission intensity value that was obtained at $\lambda = 580$ nm during titration with varying analyte concentration, $[C]$ is the concentration of Cu^{2+} or Zn^{2+} and K_a is the apparent binding constant

(M^{-1}), which was determined from the slope of the linear plot. Absorption and emission experiments were carried out using mixtures of MeCN:H₂O or DMF:H₂O (99:1, v/v).

2.3.4 Photostability studies

RBS, **RBS**– Cu^{2+} and **RBS**– Zn^{2+} solutions in THF (20 μM) were irradiated with a monochromatic xenon arc lamp at irradiances of 0.039 W/cm² and 0.052 W/cm² for 60 min. Photostability was evaluated by monitoring absorption and emission spectra as a function of time.

2.4 Fingerprint development and imaging

Fingermarks were collected from two voluntary anonymous donors and deposited on various selected substrate surfaces (i.e., smooth cell phone surface, cellotape paper, glass bottles) (Fig. S1). After the donor rubbed with their thumb or forehead/nose, it was press-stamped on the selected substrate. The sample was then immersed in **RBS**, **RBS**– Cu^{2+} and **RBS**– Zn^{2+} solution and rinsed with water or some organic solvents (acetone or ethyl acetate). The developed fingerprint was illuminated with UV lamp (365 nm) and the image recorded with a Samsung smartphone camera.

3 Results and discussions

3.1 Characterization of RBS

POSS-azide (**PA**) and rhodamine ethylenediamine dipropargyl conjugate (**RED**) were synthesized following the procedure previously reported [20, 22] (Fig. 1). That both compounds were successfully obtained was confirmed upon proper characterization and comparison with literature data (Figs. S2–S6) [20, 22]. Thereafter, the novel rhodamine bis(ethylenediamine triazolyl POSS), (i.e., **RBS**), was obtained in 82% yield by CuAAC reaction between **PA** and **RED**. ¹H NMR spectra confirmed the structure of **RBS** with evidence of bis(triazole) protons (δ 7.61 ppm, 2H) and rhodamine aromatic protons (δ 6.4–8.4 ppm, 10H) (Fig. S7). Similarly, ¹³C NMR, ²⁹Si NMR and mass spectra (Figs. S8, S9 and S10, respectively) also supported the structure of **RBS**. However, it draws attention the presence of a signal centered at 65.9 ppm in the ¹³C NMR spectrum, which indicates the closed form of the spirolactam ring (Fig. S8) [20]. The presence of 1,2,3-triazole groups in the **RBS** probe was also corroborated by FT-IR, which prominently exhibited –N=N group and –C–N bonds in addition to the characteristic Si–O–Si of the POSS (Fig. S11).

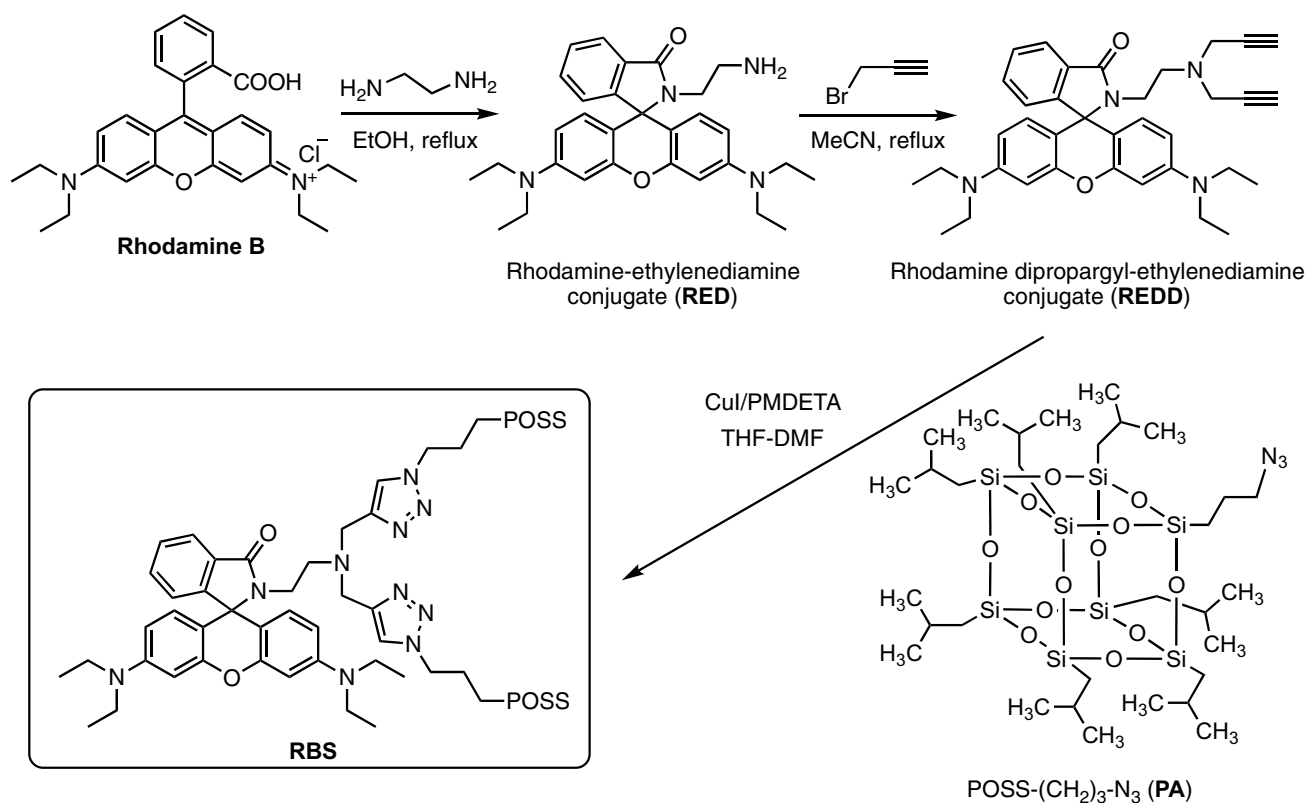


Fig. 1 Schematic procedure for the synthesis of rhodamine ethylenediamine bis(triazolyl POSS) (**RBS**)

We explored its photophysical properties in different solvents which included absorption/emission bands, molar absorption coefficients, Stokes shifts, fluorescent quantum yields, emission rate constants, singlet energies and lifetimes (Fig. S12 and Table S1). The absorption band in the UV region was clearly dominated by the rhodamine-type chromophore. Values of Stokes shifts were found to be solvent dependent, being markedly higher for polar media. Regarding fluorescence quantum yields (ϕ_F), **RBS** presented extremely poor values in all solvents in comparison with the parental rhodamine B (for instance, $\phi_F = 0.40$ in acetonitrile) [12]. This fact could be attributed to the nearby POSS moieties that may influence the radiative and non-radiative pathways of the material, with the occurrence of aggregate formation. In this sense, the emission decay traces of **RBS** were satisfactorily fitted by a biexponential function. This was in full agreement with previously reported data for similar POSS nanohybrids containing dansyl chromophores [22]. Thus, the shorter lifetimes would be ascribed to an intramolecular charge transfer (ICT) state, in which an electron transfer from the amino group to the xanthene π -system, followed by rotation of the alkyl groups was occurring [29]. Meanwhile, the formation of aggregates could be responsible for the longer lifetimes. As previously established for the

rhodamine dyes that can easily form aggregates in solution [30], when a locally excited (LE) state cannot be mixed with a charge transfer (CT) (or electron transfer) state, the interconversion from the LE to the CT results in fluorescence properties that are highly sensitive to steric environments, i.e., aggregation. This fact was indeed reflected in the contribution of the longer lifetime component, being the same or even higher, at moderately polar solvents, strengthening a major participation of aggregate formation. With the photophysical data in hands, **RBS** might be a potential candidate to be successfully applied as an “OFF–ON” metal sensor, since the possible coordination could evade formation of the aggregates and enhance the radiative pathways.

3.2 Metal ion sensing capability of the **RBS** probe

To establish the sensing capacity of **RBS**, we first evaluated its photophysical properties, focusing mainly on the emission property changes due to the low sensitivity that UV–visible (absorbance) measurements usually exhibit. A solution (20 μM) of **RBS** was visually colorless and almost non-fluorescent in common solvents such as THF, MeCN or *n*-hexane (HEX) (Table 1). This observation indicates the predominant existence of ring closed spirolactam form

Table 1 Fluorescent and colorimetry data of **RBS** in sensing Cu^{2+} and Zn^{2+}

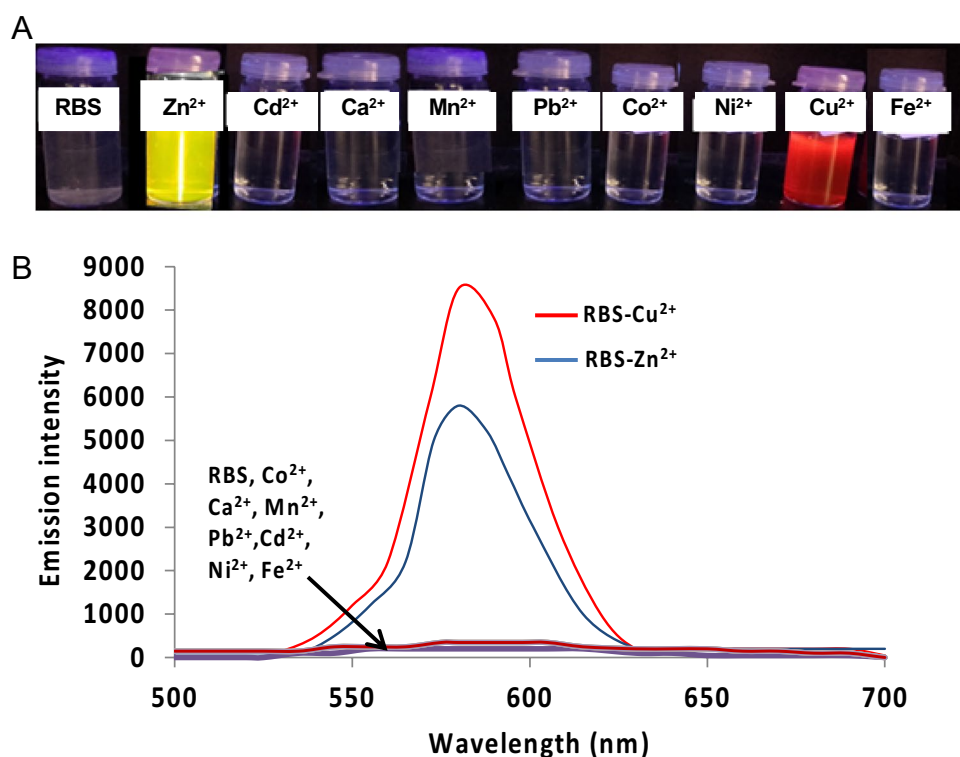
Sample	λ_{abs} max	$\lambda_{\text{f.}}$ max	Solvent (ϕ_{F})	BC	LOD fluorescence	LOD colorimetry	Sensing mode (color)	$F(\tau)/\text{ns}$	Recovery (%)
RBS	NA	NA	THF MeCN HEX	NA	NA	NA	NA	NA	NA
RBS- Cu^{2+}	468	580	THF (0.39) MeCN (0.41)	5.12×10^8	3.0 nM	2.14×10^{-8}	Fluorescent (reddish pink) Colorimetry (pink)	3.20	97.9 98.3
RBS- Zn^{2+}	427	578	HEX (0.18) THF (0.22) MeCN (0.34)	3.6×10^8	3.0 nM	4.0×10^{-8}	Fluorescent (yellowish green) Colorimetry (yellowish green)	1.68	98.6 94.4
[RBS- Cu^{2+}]+ Zn^{2+}	472	582	HEX (0.17) MeCN (0.47)	–	NA	NA	Fluorescent (yellowish green)	2.40	

[20]. Upon separate addition of several metal ion solutions to **RBS**, only Cu^{2+} and Zn^{2+} exhibited a strong fluorescent band (580 nm) with Cu^{2+} having stronger emission band (Fig. 2). Under incremental addition of Cu^{2+} to **RBS**, the

absorption spectra supported the fluorescence spectra as shown in Fig. S13.

This observation indicates that only Cu^{2+} and Zn^{2+} from among the tested metal ions could coordinately chelate with **RBS** and, eventually, emit reddish pink and yellowish green

Fig. 2 **A** Photographic images and fluorescent responses of **RBS** (20 μM) in the presence of various metal ions. **B** Fluorescent changes of **RBS** upon addition of various metal ions (10 μM)



fluorescence, respectively. **RBS**– Cu^{2+} and **RBS**– Zn^{2+} with enhanced fluorescent profiles corroborated with a 63.3-fold (0.41) and 48.3-fold (0.29) enhanced quantum yield when compared with the highest achieved by **RBS** in MeCN (Table 1). These results provide a platform for Cu^{2+} and Zn^{2+} sensing in either biological or environmental condition accompanied by structural transformation occasioned by ring opening of the spirocyclic unit via a “turn-on” chelation-enhanced fluorescent (**CHEF**) mechanism [31]. It is worth mentioning that we also tested additional monovalent and trivalent ions (i.e., Al^{3+} , Fe^{3+} , Cr^{3+} , Na^+ , Ag^+ and K^+). However, titration experiments resulted in non-coordinated uncomplexed colloidal suspensions, which made further photophysical experiments rather difficult. Therefore, we limited in this study the probe responses to representative divalent metal ions shown in Fig. 2A.

Due to the overriding sensing performance of **RBS** for Cu^{2+} , we performed titration experiments. The results indicated that the probe displays significant “turn-on” responses upon incremental addition of Cu^{2+} (0–25 μM ranging from 0 to 10 equiv) (Fig. 3A). The corresponding absorption spectra are shown in Fig. S14.

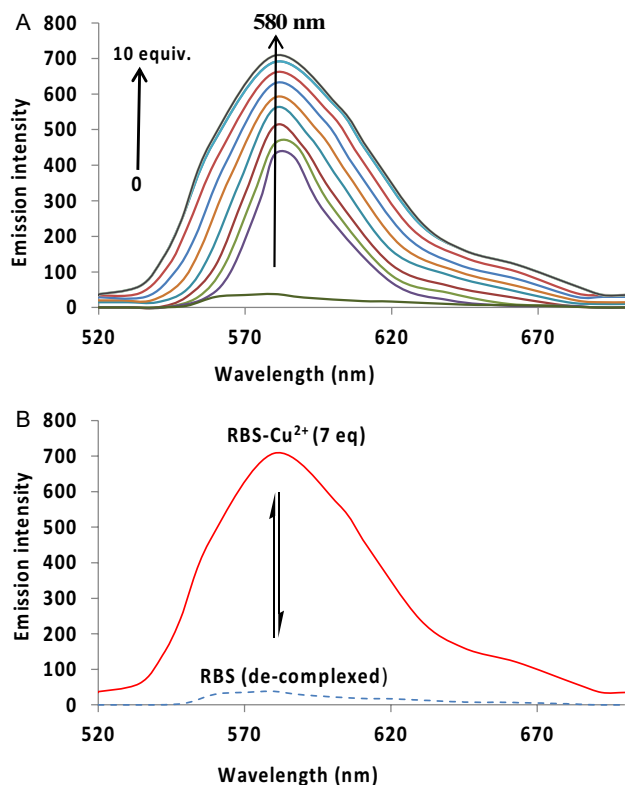


Fig. 3 **A** Fluorescent changes of **RBS** probe (20 μM) in the presence of different concentrations of Cu^{2+} . Excitation wavelength = 510 nm. **B** Reversibility of fluorescence spectra of complexed (7 equiv of Cu^{2+}) and de-complexed **RBS** following the addition of excess EDTA

The saturation point was easily reached with the addition of just 7 equiv of Cu^{2+} , indicating tight binding. However, the reversibility of, in particular, **RBS**– Cu^{2+} formation is underscored by a reversible color transition from reddish pink back to colorless upon addition of EDTA which brought down the emission intensity to the same level as in the original uncomplexed **RBS** (Fig. 3B). Thereby, the loss of the spectroscopic features of the system due to the induced decomplexation process would be indicative of the restoring of the spirocyclic form. The equilibrium interchange [14] between the open and closed spirolactam ring in reversible motif prompted by EDTA addition could be an index for monitoring metal complex formation and subsequent sensing of M^{2+} .

Among the divalent metal ions tested for **RBS** sensing, Cu^{2+} and Zn^{2+} are, undoubtedly, notable in this work. However, where both metal ions co-exist, selectivity should be an important parameter for testing the performance of a novel probe like **RBS**. In this regard, we conducted a competitive experiment by monitoring the change in fluorescent intensities at 580 nm upon addition of 5 equiv of Cu^{2+} to a solution of different metal ions (5 equiv). The results are displayed in the chart (Fig. 4A). High selectivity of **RBS** for Cu^{2+} from among all the metals tested was underscored by the significant fluorescent profile in a co-existing multi-metallic interference environment. Furthermore, confirmation of the continued selectivity and sensitivity dominance of Cu^{2+} sensing among multi-metallic interferences was further proved by the addition of **RBS**– Zn^{2+} to various cations, which did not induce any noticeable changes in the relative intensities of other metal ions except Cu^{2+} (Fig. 4B).

3.3 Dual sensing profile of **RBS**

Fluorescent transition from colorless to reddish pink and colorless to yellowish green favoring **RBS**– Cu^{2+} and **RBS**– Zn^{2+} falls within the addition of 1–7 equiv of metal ions to **RBS**. From Benesi–Hildebrand plots, we could determine the binding constants of 5.12×10^8 and 3.6×10^8 , respectively, which are high enough to justify stable **RBS**– M^{2+} bindings (Fig. 5).

The detection limit of Cu^{2+} and Zn^{2+} via fluorescent response was the same as 3.0 nM, which allows sensing of both metal ions in the nanomolar concentration range. It is noteworthy that colorimetric responses capable of being detected with the naked eye proceeded with the incremental addition of metal ions (8–10 equiv) to **RBS** (Fig. 6A). The colorimetry responses were supported by a linear relationship between the absorption intensity at 452 nm and various concentration of metal ions in the range 1–100 μM (Fig. 6B) with correlation coefficients of 0.9926 (**RBS**– Cu^{2+}) and 0.9923 (**RBS**– Zn^{2+}). The limit of colorimetric detections of **RBS** for Cu^{2+} and Zn^{2+} were

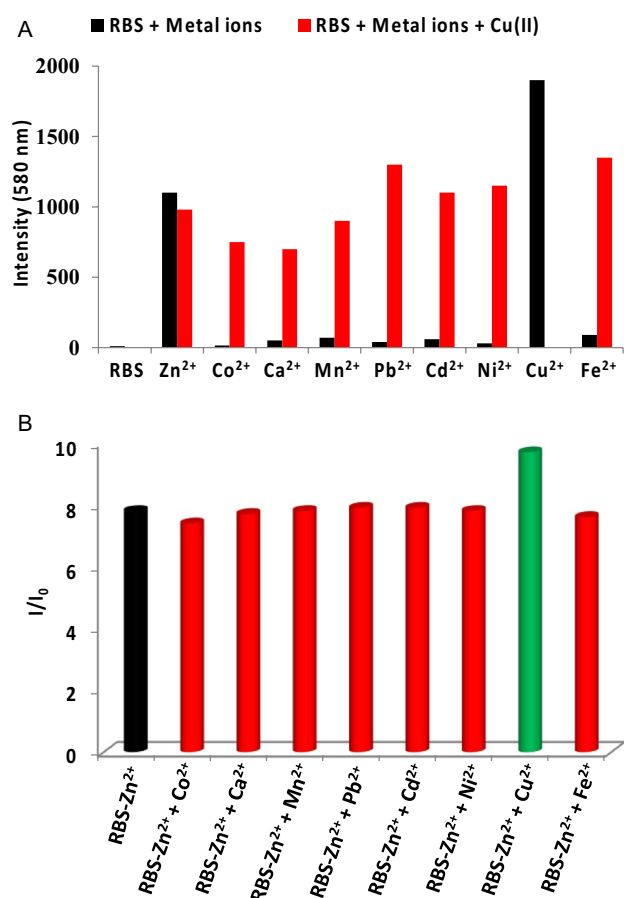


Fig. 4 **A** Fluorescent signal (580 nm) of the probe **RBS** (20 μM) to Cu²⁺ or 10 μM of other metal ions (black bar) and the mixture of other metal ions (10 μM) with 10 μM of Cu²⁺ (red bar). **B** Relative fluorescence of RBS–Zn²⁺ (20 μM) in the presence of various metal ions (10 μM). Margin of experimental error = 5%

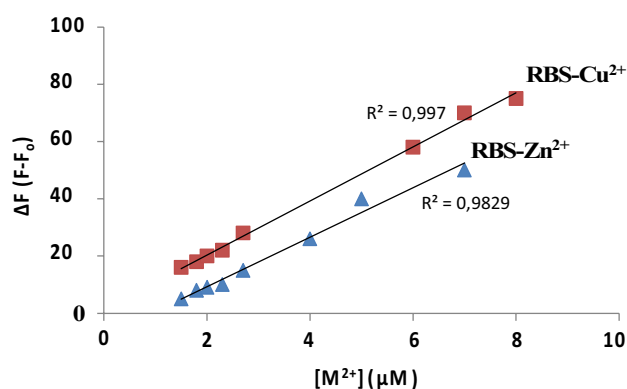


Fig. 5 Plots of fluorescent changes at 580 nm of **RBS** in the presence of Cu²⁺ or Zn²⁺. The LOD of Cu²⁺ and Zn²⁺ were calculated using the equation: LOD = 3σ/slope; σ is the standard deviation of the blank solution. Margin of experimental error = 5%

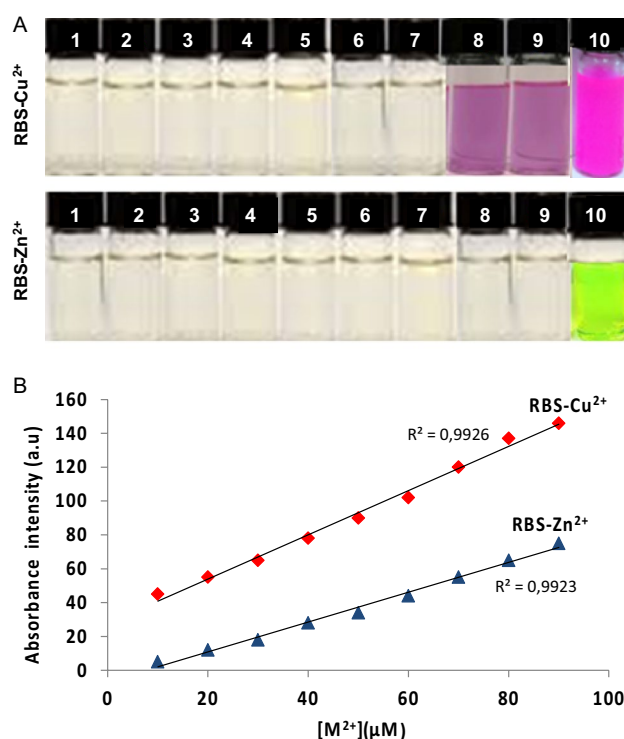


Fig. 6 **A** RBS colorimetric response during detection of Cu²⁺ and Zn²⁺ at different metal concentrations (from left to right: 1–10 equiv). **B** A linear relationship between absorbance intensity at 468 nm and concentrations of M²⁺ (Cu²⁺ and Zn²⁺). Margin of experimental error = 5%

2.14×10^{-8} and 4.0×10^{-8} mol L^{−1}, respectively. Hence, the results obtained, to a large extent, validate the reliability and practicality of the established dual-mode colorimetry and fluorescent sensing of Cu²⁺ and Zn²⁺. Furthermore, the dual-mode sensing of Cu²⁺ and Zn²⁺ by RBS was compared with a series of previously reported probes (Table 2). In general, results shown in this work are encouraging and superior in some cases.

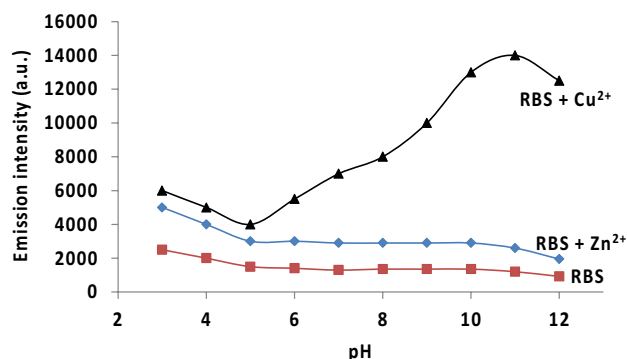
3.4 Stability profile of RBS in sensing Cu²⁺ and Zn²⁺

Photo and chemical stability are major pre-requisites for any chemosensor to be considered for biological and environmental applications [35]. Thus, we determined the stability of RBS–Cu²⁺ and RBS–Zn²⁺ over the physiologically relevant pH range (1–12) (Fig. 7). Only RBS–Cu²⁺ was found to be strongly pH dependent and recorded relatively weak fluorescent decline up to pH 5. However, there was an exponential increase in fluorescence up to pH 11, indicating that proper pH is a pre-condition for bio-application of RBS–Cu²⁺. On the other hand, neither RBS nor RBS–Zn²⁺

Table 2 Comparison of other probes for Cu^{2+} and Zn^{2+} sensing with the probe reported in this work

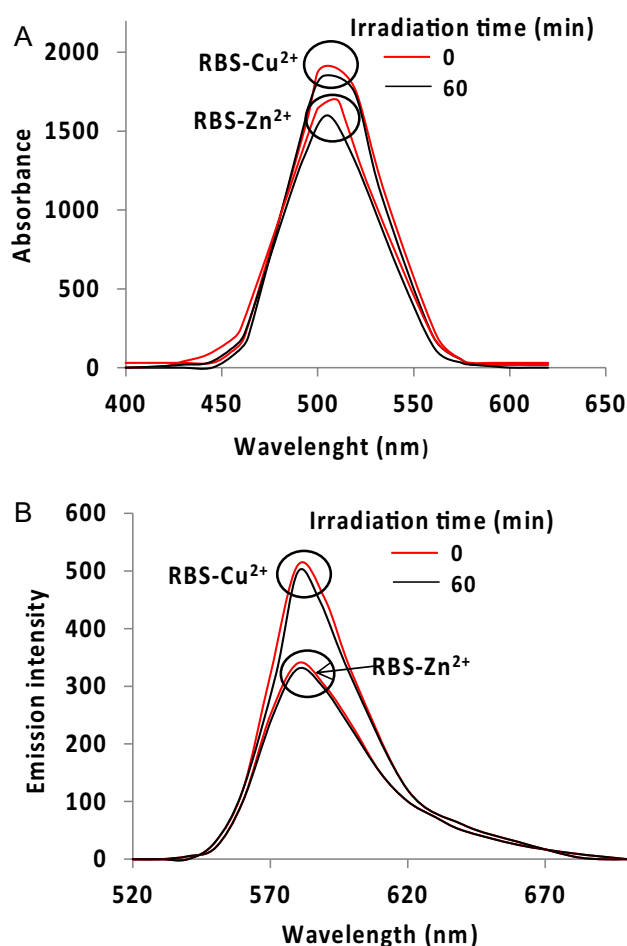
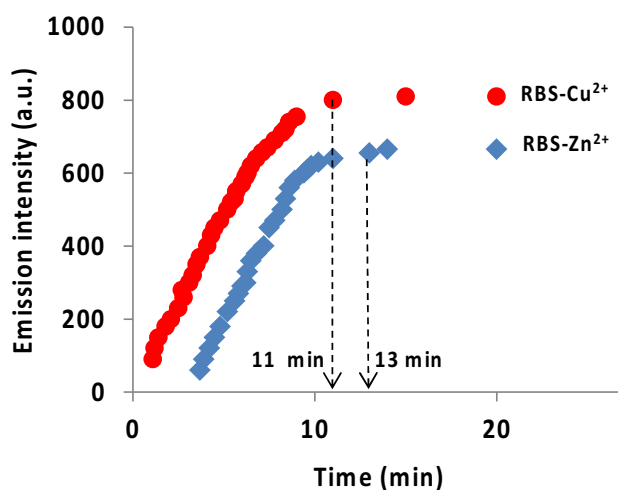
Recognition/mode	Probe based	LOD (M)	References
Cu^{2+}/F	Rhodamine	1.0×10^{-9}	[32]
Zn^{2+}/F	Rhodamine	1.0×10^{-6}	[20]
Cu^{2+}/F	Rhodamine	1.16×10^{-9}	[33]
Zn^{2+}/F	Fluorescein	3.36×10^{-7}	[34]
Cu^{2+}/C	Fluorescein	2.19×10^{-6}	[34]
Cu^{2+}/C	Schiff base	7.1×10^{-8}	[9]
Cu^{2+}/F	Schiff base	3.8×10^{-8}	[9]
Zn^{2+}/F	Schiff base	7.69×10^{-9}	[10]
Cu^{2+}/C	Schiff base	5.35×10^{-9}	[10]
Cu^{2+}/F	Rhodamine-POSS	3.0×10^{-9}	This work
Zn^{2+}/F	Rhodamine-POSS	3.0×10^{-9}	This work
Cu^{2+}/C	Rhodamine-POSS	2.14×10^{-8}	This work
Zn^{2+}/C	Rhodamine-POSS	4.0×10^{-8}	This work

F fluorescent mode, C colorimetry mode

**Fig. 7** Fluorescent emission of **RBS- Cu^{2+}** and **RBS- Zn^{2+}** over a range of pH. Margin of experimental error = 5%

was pH dependent, showing that **RBS** could not be used for Zn^{2+} detection under physiologically aqueous conditions. More detailed experiments are yet necessary to unequivocally correlate protonation/deprotonation rate constants and/or induction of molecular aggregation with the emission intensity profile over the pH scale for the different complexes.

Secondly, to establish the photostability profile, we irradiated a solution of **RBS- Cu^{2+}** and **RBS- Zn^{2+}** at 356 nm up to 60 min. The absorption and emission as a consequence of the irradiation are comparatively illustrated in Fig. 8. As it can be observed, **RBS** in its complex formation is adequately photostable in sensing both Cu^{2+} and Zn^{2+} , as there are no significant absorption and emission changes at their respective maximum band peaks.

**Fig. 8** Photostability profile: **A** colorimetry/absorption and **B** fluorescence spectra of **RBS** in sensing Cu^{2+} and Zn^{2+} under photo-irradiation at time interval**Fig. 9** Time-dependence plots of fluorescent changes at 580 nm of **RBS** (20 μM) upon addition of Cu^{2+} or Zn^{2+} . Margin of experimental error = 5%

Along with the adequate photostability shown by RBS in sensing Cu^{2+} and Zn^{2+} , the fast sensing response time toward these metal ions should also be highlighted, within 11 and 13 min, respectively, and keeping constant thereafter for a reasonable period of time (Fig. 9).

Additionally, the excited state of **RBS**– Cu^{2+} and **RBS**– Zn^{2+} showed adequate lifetime within 3.20 ns and 1.68 ns, respectively, which equally signified sensing stability (Table 1). The recovery of both fluorimetry and colorimetry detections of Cu^{2+} and Zn^{2+} is on the high side (96.4–98.3%; values calculated from Fig. 8 = $[\text{max} - \text{min}] / [\text{min}] \times 100$) (Table 1), corroborating the good stability, reliability and practicality of the dual sensing properties of **RBS** for these metal ions. These results underpinned to a large extent earlier studies [21, 22], reiterating triazolyl-POSS with scavenging photodegradation. Our designed bis-triazolyl-POSS anchoring rhodamine enhanced the photostability as a result of the strong binding profile of bis-triazoles to metal ions. The folding tendency of the triazole unit toward metal coordination depends on the bulkiness of the group at the terminal. In this sense, the inclusion of large POSS units facilitates the folding over the diamino linker favoring a stronger metal coordination.

3.5 Coordination sensing mechanism

The observed dual-mode visually prompted by fluorescent and colorimetric responses of **RBS** to Cu^{2+} and Zn^{2+} occasioned, undoubtedly, the plausible binding modes vis-à-vis structural orientation as detailed in Fig. 10. Job's plot indicates that **RBS**– Cu^{2+} and **RBS**– Zn^{2+} have preferences for 2:1 and 1:1 binding stoichiometry, respectively (Fig. 11). The observed discrepancy in the binding stoichiometry suggests different binding orientations with respect to bis-triazole ($-\text{N}=\text{N}-\text{Cu}-\text{N}=\text{N}-$) and open spirolactam carbonyl of the amide/triazole ($\text{O}-\text{Cu}-\text{N}=\text{N}$). Plausibly, once the Cu^{2+} or Zn^{2+} is fixed in the cavity of **RBS** via the coordination–bonding interaction, the electron cloud on the electron-rich imine fragment will transfer to the large rhodamine ring system resulting in the ring opening of spirolactam amide to form a five-member or six-member ring [36]. The exclusive sensing of Cu^{2+} and Zn^{2+} owes to the stronger ability of these ions toward the ligand due to the optimal size of **RBS** cavity. We can further explain this phenomenon based on hard and soft acid and base interaction (HSAB) theory [36, 37] and chelation size [38], since Cu^{2+} and Zn^{2+} have

comparable chelating sizes. The predominating selectivity of **RBS** for Cu^{2+} is based on an analogy that the metal ion is a hard acid, which preferentially opts for a stronger “N” hard base in the triazole moiety [35].

As predicted, **RBS** was much more selective for Cu^{2+} than Zn^{2+} and free from cross reactivity with other competing metal ions. It should also be considered that an interference of Zn^{2+} could be significant where Cu^{2+} and Zn^{2+} co-exist in analytical samples for physiological applications. This prompted us to carry out further dual metal system experiments. The addition of Zn^{2+} to the **RBS**– Cu^{2+} resulted in a 2.1-fold fluorescent intensity (see Fig. 10, inset). Such enhancement may be due to the addition of Zn^{2+} , which possesses the tendency to displace Cu^{2+} from the triazole–triazole ($\text{N}=\text{N}-\text{Cu}-\text{N}=\text{N}$) coordination and, eventually, opt for amide–triazole ($\text{O}-\text{Cu}-\text{N}=\text{N}$) coordination. As previously proposed [39], and supporting our analogy, the folding tendency of the triazole unit moves toward the amide segment and is favorable for Zn^{2+} coordination. Furthermore, the dangling bulky triazolyl-POSS could facilitate Zn^{2+} coordination during $\text{Cu}^{2+}/\text{Zn}^{2+}$ exchange.

3.6 Deployment of the resulting **RBS**– Cu^{2+} and **RBS**– Zn^{2+} for fingerprinting imaging

Inspired by our most recent work [21, 22] where we successfully took advantage of fluorophore-triazolyl-POSS for fingerprint imaging, coupled with various reported M^{X} complexes [40–42], we considered it worthwhile to adopt the fluorescent and colorimetric attributes of **RBS**– M^{2+} in fingerprint imaging. For these studies, fingerprints of selected donors were imaged and detected via both fluorescent and colorimetric responses of **RBS**– Cu^{2+} and **RBS**– Zn^{2+} with high sensitivity, selectivity and legibility (Fig. 12).

Detailed observation of the ridge features showed Whorl, bifurcation and ridge ending, which to a large extent fulfill the requirements of fingerprint identifications in forensic science.

A judicious balance of hydrophobic and π – π interactions have been recognized in previous reports [21, 22]. Accordingly, **RBS**– M^{2+} was designed to possess multiple binding profiles which are subsequently available for interaction with the $-\text{C}=\text{O}$ and $-\text{NH}_2$ of amino acids in fingerprint oils (Fig. 13). The whole ensemble, which consists of **RBS**– M^{2+} in non-covalent interactions with $-\text{C}=\text{O}$ and $-\text{NH}_2$, formed a ternary complex that cooperatively work

to provide stabilized fingerprint detection and eventual imaging. Some fluorescent chemosensor systems have been developed to detect amino acids based on probe–metal ion ensembles [15]. Importantly, brightness, contrast and visual legibility remained unchanged up to 1 year, when

developed with **RBS–Cu²⁺** under fluorescent response (2 equiv of Cu²⁺). However, dimmer and less contrast pink and green images surfaced at the end of the 6th month for **RBS–Cu²⁺** and **RBS–Zn²⁺**, respectively, when colorimetric responses (10 equiv) predominate.

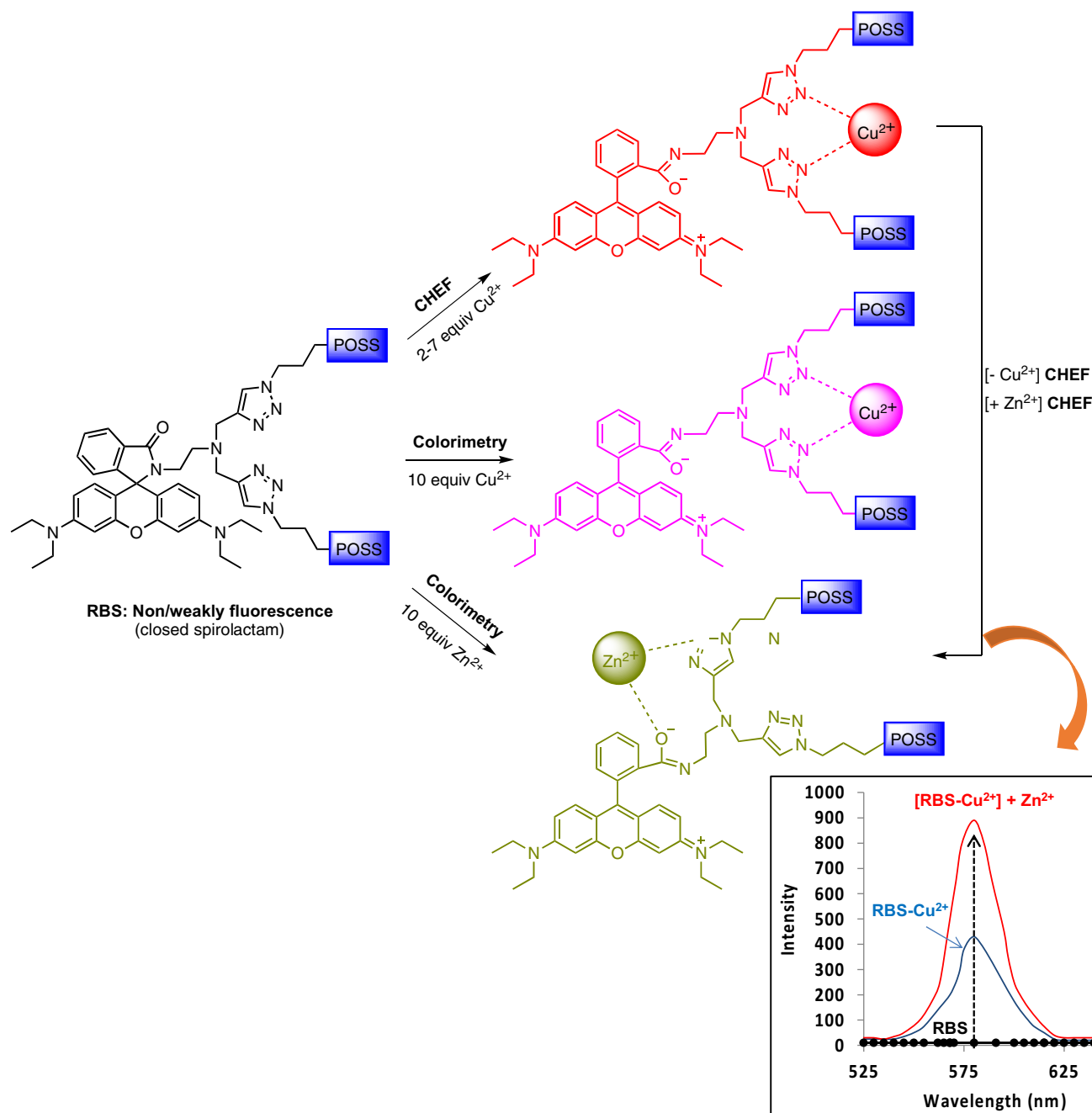


Fig. 10 Plausible dual sensing and binding mechanisms of **RBS** with Cu²⁺ or Zn²⁺. Inset: Fluorescence intensity changes of **RBS–Cu²⁺** and **[RBS–Cu²⁺] + Zn²⁺** ($\lambda_{\text{exc}} = 510 \text{ nm}$): **RBS** (20 μM) + Cu²⁺ (10 equiv) + Zn²⁺ (10 equiv) in MeCN (99:1, v/v)

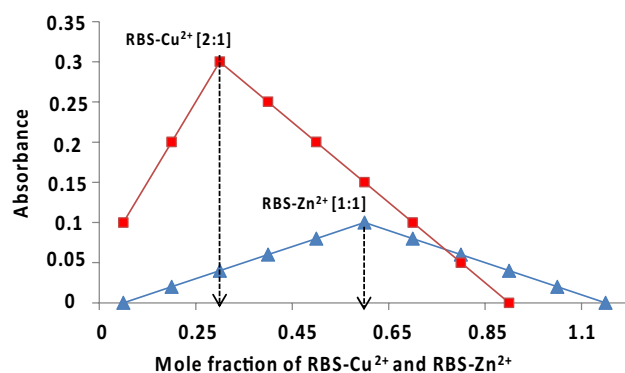


Fig. 11 Job's plots for **RBS-Cu²⁺** and **RBS-Zn²⁺** indicating stoichiometry 2:2 and 1:1, respectively. Margin of experimental error = 5%

We could ascribe the apparently lesser short-lived and dimmer image features obtained under colorimetric responses to unhidden open images that are frequently exposed to light, which eventually fade the pink and yellowish green fingerprint images over time. Obviously, the latent nature of fingerprint developed by fluorescent **RBS-Cu²⁺** (2 equiv) forestalls frequent exposure to light and eventually

confers extra stability to the reddish pink fingerprint image which spanned over 12 months.

4 Conclusion

We have established a “turn-on” type of **CHEF** and colorimetric sensor for **Cu²⁺** and **Zn²⁺**, respectively, using a novel **RBS** derivative. The binding pattern for **RBS-Cu²⁺** (2:1) and **RBS-Zn²⁺** (1:1) exist by coordination of the corresponding metal ions with triazole–triazole and triazole–amide moieties. Competitive experiments with **RBS-Cu²⁺** showed that the addition of **Zn²⁺** could displace **Cu²⁺** by triggering a fluorescent enhancement (2.1-fold). The synthetic design of the **RBS** sensor was modular, being possible to further attach a number of other fluorophores using “click” chemistry while creating a library of **M²⁺** sensors with different excitations, absorptions and emission wavelength. This is the first example of a bis-triazolyl-POSS conjugate anchoring on rhodamine. Therefore, one can envisage other uses for such a generic system in chemical sensing

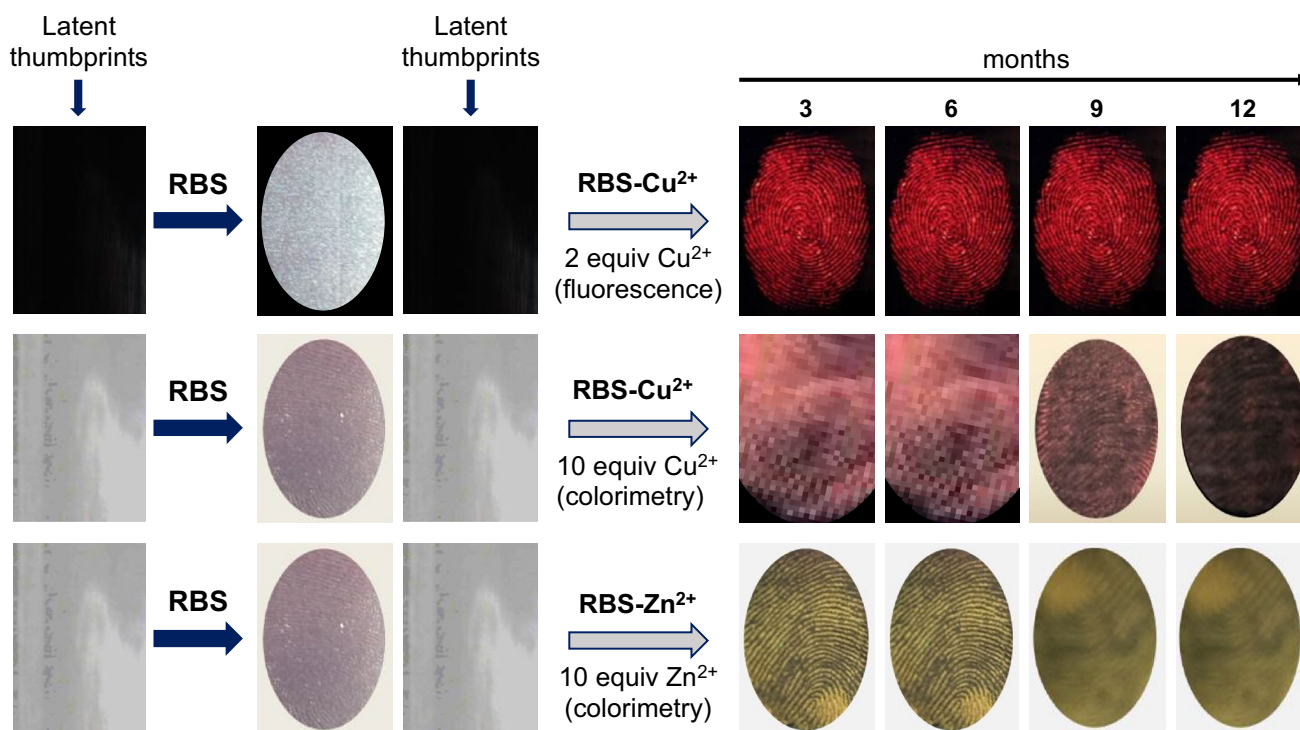


Fig. 12 Fingerprint detections and images captured under fluorescent and colorimetry responses of **RBS-Cu²⁺** and **RBS-Zn²⁺**

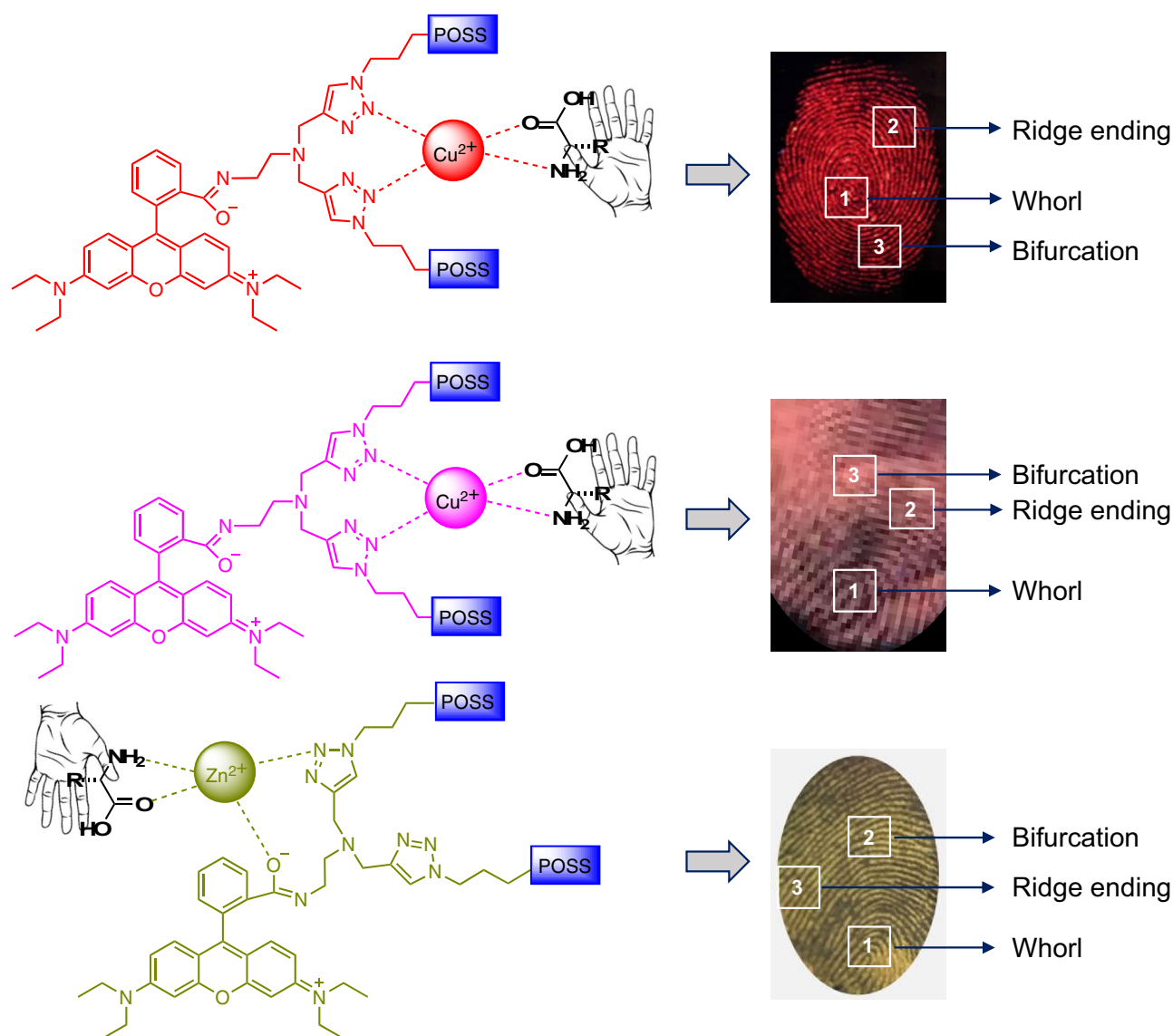


Fig. 13 Proposed mechanism of fingerprint formation based on $[\text{RBS-M}^{2+}]$ –finger amino acid interactions

vis-à-vis coordination chemistry. Furthermore, we used a novel application of the resultant RBS-M^{2+} for fingerprinting detection vis-à-vis imaging with promising sensitivity, stability and legibility.

Supplementary Information The online version contains supplementary material available at <https://doi.org/10.1007/s43630-023-00395-4>.

Acknowledgements E.O. Dare thanks Alexander von Humboldt Foundation for Georg Forster Research Fellowship. Funding from Generalitat Valenciana (CIDEGENT/2018/044) is acknowledged. The Institute of Organic Chemistry, Regensburg University, Germany and the Chemistry Department, UPV, Spain graciously provided laboratory space and facilities. D.D.D. thanks the Spanish Government for the Senior Beatriz Galindo Award (BEAGAL18/00166), financial support from the Spanish Government (PID2019-105391GB-C21/

AEI/10.13039/501100011033) and NANOTec, INTech, Cabildo de Tenerife and ULL for the laboratory facilities.

Funding Open Access funding provided thanks to the CRUE-CSIC agreement with Springer Nature.

Data availability All data generated or analysed during this study are included in this published article and its supplementary information files.

Declarations

Conflict of interest On behalf of all authors, the corresponding author states that there is no conflict of interest.


Open Access This article is licensed under a Creative Commons Attribution 4.0 International License, which permits use, sharing, adaptation, distribution and reproduction in any medium or format, as long as you give appropriate credit to the original author(s) and the source, provide a link to the Creative Commons licence, and indicate if changes were made. The images or other third party material in this article are included in the article's Creative Commons licence, unless indicated otherwise in a credit line to the material. If material is not included in the article's Creative Commons licence and your intended use is not permitted by statutory regulation or exceeds the permitted use, you will need to obtain permission directly from the copyright holder. To view a copy of this licence, visit <http://creativecommons.org/licenses/by/4.0/>.

References

- Ganesh, C. M., Sushovan, P., Sudipta, B., Subhadeep, S., & Jyotirmayee, D. (2013). Design and synthesis of an on-off fluorophore that executes a logic operation and detects heavy and transition metal ions in water and living cells. *Organic & Biomolecular Chemistry*, 11, 3057–3063.
- Isarankura-Na-Ayudhya, C., Tantimongkolwat, T., Galla, H. J., & Prachayasittikul, V. (2010). Fluorescent protein-based optical biosensor for copper ion quantitation. *Trace Elem. Res.*, 134, 352–365.
- Hu, M., Li, H., Chen, L., Zhang, H., & Dong, C. (2009). Fluorescence quenching of pheophytin-a by copper(II) ions. *Chinese Journal of Chemistry*, 27, 513.
- Luo, H. Y., Zhang, H. B., Jiang, J. H., Li, C. Y., Peng, J., Shen, L., & Yu, R. Q. (2007). An optode sensor for Cu^{2+} with high selectivity based on porphyrin derivative appended with bipyridine. *Analytical Sciences*, 23, 551.
- Geng, H., Xuel, L., Wanme, L., Wenz, T., Tian, Y., Jian, L., & Wang, Z. (2022). Carbon dots based multicolor fluorescence sensor for ratiometric and colorimetric dual-model detection of Cu^{2+} . *Dyes and Pigments*, 203, 110381.
- Sahu, S., Sikdar, Y., Bag, R., Cerezo, J., Cerón-Carrasco, J. P., & Goswami, S. (2022). Turn on fluorescence sensing of Zn^{2+} based on fused isoindole-imidazole scaffold. *Molecules*, 27, 2859.
- Sasan, S., Chopra, T., Gupta, A., Tsering, D., Kapoor, K. K., & Parkesh, R. (2022). Fluorescence “turn-off” and colorimetric sensor for Fe^{2+} , Fe^{3+} , and Cu^{2+} ions based on a 2,5,7-triarylimidazopyridine scaffold. *ACS Omega*, 7, 11114–11125.
- Ramakrishnan, A., Krishna, S., & Sivan, V. (2022). A review on fluorimetric and colorimetric detection of metal ions by chemodosimetric approach 2013–2021. *Coordination Chemistry Reviews*, 459, 214401.
- Memar, S., Amit, K., Manna, G., & Kumar, P. (2022). A fluorescent colorimetric vanillin di-Schiff base chemosensor for detection of Cu(II) and isolation of trinuclear Cu(II)–dihydrazide. *Mater. Adv.*, 3, 2495–2504.
- Anjitha, J., Gayathri, G., Sivaraman, C., & Ayya, S. (2022). A highly potential acyclic Schiff base fluorescent turn on sensor for Zn^{2+} ions and colorimetric chemosensor for Zn^{2+} , Cu^{2+} and Co^{2+} ions and its applicability in live cell imaging. *Journal of Photochemistry and Photobiology B: Biology*, 226, 112371.
- Grimm, J. B. (2017). A general method to fine-tune fluorophores for live-cell and in-vivo imaging. *Nature Methods*, 14, 987–994.
- Zheng, Q. (2019). Rational design of fluorogenic and spontaneous blinking labels for super-resolution imaging. *ACS Central Science*, 5, 1602–1603.
- Wang, L. (2020). A general strategy to develop cell permeable and fluorogenic probes for multi-colour nanoscopy. *Nature Chemistry*, 12, 165–172.
- Chi, W., Qi, Q., Lee, R., Xu, Z., & Liu, X. (2020). A unified push-pull model for understanding the ring-opening mechanism of rhodamine dyes. *Journal of Physical Chemistry C*, 124, 3793–3801.
- Heejeong, M., Jinyoung, P., & Jinsung, T. (2016). Fluorescent probes based on rhodamine hydrazides and hydroxamates. *Chemical Record*, 16, 124–140.
- Farid, A., & Hai, X. (2021). Recent developments in 1,2,3-triazole-based chemosensors. *Dyes and Pigments*, 185, 108905.
- Kumar, A., Chae, P. S., & Kumar, S. (2020). A dual-responsive anthrapyridone-triazole-based probe for selective detection of Ni^{2+} and Cu^{2+} : A mimetic system for molecular logic gates based on color change. *Dyes and Pigments*, 174, 108092.
- Ghosh, D., Rhodes, S., Winder, D., Atkinson, A., Gibson, J., & Ming, W. (2017). Spectroscopic investigation of bis-appended 1,2,3-triazole probe for the detection of Cu(II) ion. *Journal of Molecular Structure*, 1134, 638–648.
- Wu, C., Ikejiri, Y., Zhao, J.-L., Jiang, X.-K., Ni, X.-L., & Zeng, X. (2016). A pyrene-functionalized triazole-linked hexahomotrioxacalix[3]arene as a fluorescent chemosensor for Zn^{2+} ions. *Sensors and Actuators B: Chemical*, 228, 480–485.
- Wechakorn, K., Suksen, K., Piyachaturawat, P., & Kongsaree, P. (2016). Rhodamine-based fluorescent and colorimetric sensor for zinc and its application in bioimaging. *Sensors and Actuators, B: Chemical*, 228, 270–277.
- Dare, E. O., Vendrell-Criado, V., Jiménez, M. C., Pérez-Ruiz, R., & Díaz Díaz, D. (2020). Novel fluorescent labeled octasilsesquioxanes nanohybrids as potential materials for latent fingerprinting detection. *Chemistry—A European Journal*, 26, 13142–13146.
- Dare, E. O., Vendrell-Criado, V., Jiménez, M. C., Pérez-Ruiz, R., & Díaz Díaz, D. (2021). Highly efficient latent fingerprint detection by eight-dansyl-functionalized octasilsesquioxane nanohybrids. *Dyes and Pigments*, 184, 108841–108848.
- Cordes, D. B., Lickiss, P. D., & Rataboul, F. (2010). Recent developments in the chemistry of cubic polyhedral oligosilsesquioxanes. *Chemical Reviews*, 110, 2081–2173.
- Lin, M., Luo, C., Xing, G., Chen, L., & Ling, Q. (2017). Influence of polyhedral oligomeric silsesquioxanes (POSS) on the luminescence properties of non-conjugated copolymers based on iridium complex and carbazole units. *RSC Advances*, 7, 39512–39522.
- Dong, F., Lu, L., & Ha, C. (2019). Silsesquioxane-containing hybrid nanomaterials: Fascinating platforms for advanced applications. *Chemical Physics*, 220, 1800324.
- Du, Y., & Liu, H. (2020). Cage-like silsesquioxane based hybrid materials. *Dalton Transactions*, 17, 5396–5405.
- Shi, H., Yang, J., You, M., Li, Z., & He, C. (2020). Polyhedral oligomeric silsesquioxanes (POSS)-based hybrid soft gels: Molecular design, material advantages, and emerging applications. *ACS Materials Letters*, 2, 296–316.
- Benesi, H. A., & Hildebrand, J. H. (1949). A spectrophotometric investigation of the interaction of iodine with aromatic hydrocarbon. *Journal of the American Chemical Society*, 71, 2703–2707.
- Lopez Arbeloa, F., Lopez Arbeloa, T., Tapia Estevez, M. J., & Lopez Arbeloa, I. (1991). Photophysics of rhodamines: Molecular structure and solvent effects. *Journal of Physical Chemistry*, 95, 2203–2208.
- Tajalli, H., Ghanadzadeh Gilani, A., Zakerhamidi, M. S., & Moghadam, M. (2009). Effects of surfactants on the molecular

- aggregation of rhodamine dyes in aqueous solutions. *Spectrochimica Acta Part A*, 72, 697.
31. Liu, H.-M., Venkatesan, P., & Wu, S.-P. (2014). A sensitive and selective fluorescent sensor for zinc(II) and its application to living cell imaging. *Sensors and Actuators, B: Chemical*, 203, 719–725.
 32. Wechakorn, K., Prabpai, S., Suksen, K., Kanjanasirirat, P., Pewkliand, Y., Borwornpino, S., & Kongsaree, P. (2017). A rhodamine-triazole fluorescent chemodosimeter for Cu²⁺ detection and its application in bioimaging. *Luminescence*, 33, 64–70.
 33. Gauthama, B. U., Narayana, B., Sarogini, B. K., Kodlady, S. N., Sangappa, Y., & Raghu, S. V. (2022). A versatile rhodamine B-derived fluorescent probe for selective Cu²⁺ sensing. *Inorganic Chemistry Communications*, 141, 109501.
 34. Sun, J., Tian-rong, L., Cong, L., & Zheng-yin, Y. (2021). A dual probe for selective sensing of Zn²⁺ by fluorescent and Cu²⁺ by colorimetric methods in different system based on 7,8-benzochromone-3-carbaldehyde-(fluorescein) hydrazine. *Journal of Photochemistry and Photobiology A: Chemistry*, 406, 113007.
 35. Narendra, R. C., Sathiah, T., & Asit, B. M. (2012). A new triazole appended rhodamine chemosensor for selective detection of Cu²⁺ ions and live-cell imaging. *Sensors and Actuators B*, 171–172, 294–301.
 36. Zhengquan, Y., Gang, W., Shanyi, G., Manman, X., Xia, R., Rongliang, W., Gang, Z., Fuyou, K., & Hongyao, X. (2018). A multidentate ligand chromophore with rhodamine-triazole-pyridine units and its acting mechanism for dual-mode visual sensing trace Sn²⁺. *Dyes and Pigments*, 159, 542–550.
 37. Wang, Y., Huang, Y., Li, B., Zhang, L., Song, H., Jiang, H., & Gao, J. (2011). A cell compatible fluorescent chemosensor for Hg²⁺ based on a novel rhodamine derivative that works as a molecular keypad lock. *RSC Advances*, 1, 1294–1300.
 38. Zhao, Y., Zhang, X. B., Han, Z. X., Qiao, L., Li, C. Y., Jian, L. X., Shen, G. L., & Yu, R. Q. (2009). Highly sensitive and selective colorimetric and off-on fluorescent chemosensor for Cu²⁺ in aqueous solution and living cells. *Analytical Chemistry*, 81, 7022–7030.
 39. Balamurugan, R., Chih-Chieh, C., Cheng, C., & Jui-Hsiang, L. (2013). Fluorogenic and chromogenic detection of Cu²⁺ and Fe³⁺ species in aqueous media by rhodamine-triazole conjugate. *Tetrahedron*, 69, 235–241.
 40. Singh, R., & Parameswaran, P. (2022). Mono- and rare trinuclear Zn(II) complexes with near-infrared emissive ligands: Anion-responsive nuclearity control, interconversion, solid-state NIR emission, and latent fingerprint imaging. *Crystal Growth & Design*, 22, 2910–2924.
 41. Yi, K., Li, H., Zhang, X., & Zhang, L. (2021). Designed Tb(III)-functionalized MOF-808 as visible fluorescent probes for monitoring bilirubin and identifying fingerprints. *Inorganic Chemistry*, 60, 3172–3180.
 42. Tong, W., Jiachen, H., Le, W., Jiaqi, T., Hu, Z., Da, X., Sijing, S., Chao, F., Wengang, B., & Chun, S. (2021). Magnetic perovskite nanoparticles for latent fingerprint detection. *Nanoscale*, 13, 12038–12044.

Authors and Affiliations

Enock O. Dare^{1,2} · Temilade F. Akinhanmi¹ · J. A. Aremu¹ · Olayide R. Adetunji^{1,6} · Janet T. Bamgbose¹ · Victoria Vendrell-Criado³ · M. Consuelo Jiménez³ · Raúl Pérez-Ruiz³ · Sebastian Bonardd^{4,5} · David Díaz Díaz^{2,4,5} 

✉ Enock O. Dare
dareeo@funaab.edu.ng

✉ David Díaz Díaz
ddiazdiaz@ull.edu.es

¹ Department of Chemistry, Federal University of Agriculture, Abeokuta, Nigeria

² Institute of Organic Chemistry, Faculty of Chemistry and Pharmacy, Regensburg University, Regensburg, Germany

³ Departamento de Química, Universitat Politècnica de València, Camino de Vera, s/n, 46022 Valencia, Spain

⁴ Departamento de Química Orgánica, Universidad de la Laguna, Avda. Astrofísico Francisco Sánchez 3, 38206 La Laguna, Tenerife, Spain

⁵ Instituto Universitario de Bio-Organica Antonio González, Universidad de la Laguna, Avda. Astrofísico Francisco Sánchez 2, 38206 La Laguna, Tenerife, Spain

⁶ Department of Mechanical Engineering, Federal University of Agriculture Abeokuta, Abeokuta, Nigeria